https://doi.org/10.5194/amt-2022-302
Preprint. Discussion started: 6 December 2022

Atmospheric Measurement Techniques Discussions

Doppler power spectrum processing methods for a vertical sensing 94 GHz millimeter-wavelength cloud radar

Hai Lin[1,2], Jie Wang[1,2], Zhenhua Chen[1,2,3], and Junxiang Ge[1,2,3]

[1]School of Electronic and Information Engineering, Nanjing University of Information Science & Technology, Jiangsu 210044, China
[2]Institute of Electronics Information Technology and System, Nanjing University of Information Science and Technology, Nanjing 210044, China
[3]Jiangsu Key Laboratory of Meteorological Observation and Information Processing, Jiangsu 210044, China

Correspondence: Junxiang Ge (jxge@nuist.edu.cn)

Abstract. A set of Doppler power spectrum processing methods for TJ-II, a vertical sensing 94 GHz millimeter-wave cloud radar(MMCR), is proposed to distinguish clouds and enhance the data quality. The noise level is estimated by a modified segment method with 2-D segments. A two-step cloud signal mask method is proposed to distinguish clouds and noise. A Gaussian filter with adaptive standard variance is used to improve detection performance at the boundary of clouds and noise. Square signal blocks were constructed to test our method. Velocity dealiasing is carried out combined with a pre-dealiasing processing and the dual Pulse Repetition Frequency (PRF) technique to address a particular phenomenon called half-folded in MMCRs, which can not be fixed by post-processing at the base datum stage. Some observations of TJ-II are used to demonstrate our method. A comparison between our method as pre-processing and the method as post-processing proposed by Key Laboratory for Semi-Arid Climate Change of the Ministry of Education and College of Atmospheric Sciences, Lanzhou University, was carried out using one-day observation. It was found that our method shows some advantages in cloud base detection.

1 Introduction

Clouds cover almost two-thirds of the global surface. They are composed of water droplets, supercooled water droplets, ice crystals, and their mixtures condensed from water vapor in the atmosphere. Clouds contribute to our lives in both direct and indirect ways. Clouds are the most visible elements of the sky and the dominant contributors to the weather we experience every day. Clouds play an important role in climate change, global radiation budget, and weather forecasting(Muller and Fischer, 2007; Rosenfeld, 2006; Arking, 1991). Clouds control Earth's weather and regulate its climate(Solomon et al., 2007; Collins et al., 2007). Clouds also play a critical role in the water cycle and shape the global distribution of water resources.

Despite the importance of clouds in the climate system, they are difficult to represent in climate models(Bony et al., 2015). Clouds constitute the largest single source of uncertainty in climate prediction(Baker and Peter, 2008). Therefore, the study of clouds is integral to meteorological and climate research.

Cloud researches are complex and huge, from macroscopic cloud amount, cloud shape, cloud height, and cloud velocity detection to microscopic cloud particle physics, chemistry, optics, radiation characteristics, etc. Cloud sensing is the founda-

https://doi.org/10.5194/amt-2022-302
Preprint. Discussion started: 6 December 2022

Atmospheric Measurement Techniques Discussions

tion of cloud research. Clouds have been the subject of observation for centuries, but serious systematic investigations began only a few decades ago(Lamb and Verlinde, 2011). The current common remote sensing devices for clouds include weather radar, cloud lidar, and millimeter-wave cloud radar(MMCR)(Ran et al., 2021; McGill et al., 2002; Lhermitte, 1987a). These devices have different application scenarios. Weather radar mainly operates at S-band and C-band, such as WSR-88D, CINRAD/CC, with low atmospheric propagation loss and extremely high peak transmit power, making it the most indispensable tool for remote sensing of large-scale clouds and precipitation(Kumjian, 2018). Lidar is capable for boundary layer, Cloud-Top Height(CTH), Cloud Base Height(CBH) and aerosol sensing with high resolution(Ansmann and Müller, 2005; Baars et al., 2008; Müller et al., 2007; Kim et al., 2011; Stephens et al., 2002). On the opposite, Lidar is relatively poor at detecting thick clouds due to poor penetration.

Millimeter-wave radars(MMCR) are somewhere in between weather radar and lidar, with higher spatial and temporal resolution than weather radars and better penetration than lidar, making it the better tool for cloud vertical structure(CVS) sensing(Yan et al., 2021). Not only the macro parameters such as cloud thickness, cloud-top height, cloud-bottom height, and cloud amount but also the microphysics parameter such as cloud particle size, concentration, droplet spectrum distribution, etc. could be obtained by MMCRs(Kropfli et al., 1995; Kollias et al., 2007; Verlinde et al., 2013).

Because of its outstanding advantages for cloud research, MMCR has been deployed on various research platforms, including Cloud-Sat with Cloud Profiling Radar(CPR, Atmospheric Radiation Program (ARM) with Ka-band Zenith Radar(KAZR) .etc(Im et al., 2005; Chandra et al., 2015). The 94 GHz(W-band) and 35 GHz(Ka-band) are the common frequencies MMCRs work at. Compared with the 35 GHz, 94 GHz MMCR has a shorter wavelength with a stronger cloud particle backscatter, leading to better detection performance. 94 GHz MMCR was first developed by Lhermitte (1987a, b). Nowdays, there are a variety of 94 GHz MMCR(Takano et al., 2012; Huggard et al., 2008; Danne et al., 1999; Wu et al., 2014; Hogan et al., 2003; Delanoë et al., 2016). They almost take one of the two systems. One is Pulse Doppler(PD) radar with a Traveling Wave Tube Amplifier(TWTA) and one or two antennas. The other is Frequency Modulated Continuous Wave(FMCW) radar with a Solid-State Power Amplifier(SSPA) and two antennas. The PD MMCR always used TWTA due to the insufficient peak power of W-band SSPA in the past, while FMCW MMCR always used two antennas due to insufficient isolation of the W-band circulator. The PD MMCR with TWTA suffers from power supply requirements and lifetime. FMCW MMCR with two antennas suffers in size and weight. Benefiting from the rise in power of the 94G SSPA in recent years, to address the deficiencies of these two kinds of radars due to size, power demand, and reliability, Our team developed a PD MMCR called TianJian II(TJ-II) with a single antenna and SSPA. Naturally, a set of Doppler power spectrum processing methods matching TJ-II characteristics is proposed.

The TJ-II MMCR is described in Sect.2. A noise level estimating method based on the segment method is described in Sect.3. A cloud signal mask method with two-step is described in Sect.4. A velocity dealiasing method combined with the dual pulse repetition frequency (PRF) technique is described in Sect.5. Examples of our method applied to TJ-II observations are shown in Sect.6

https://doi.org/10.5194/amt-2022-302
Preprint. Discussion started: 6 December 2022

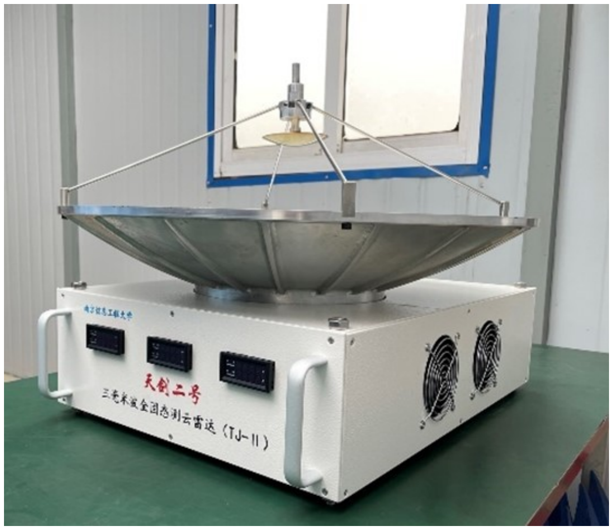

Figure 1. Photo of TJ-II MMCR

2 The TJ-II radar

TJ-II cloud radar, developed by Nanjing University of Information Science & Technology(NUIST), is a groud-base vertical detection cloud radar. It works at about 94 GHz for dual-polarization measurements. It is a PD radar using SSPA and has only a single antenna with two polarized ports(Wang et al., 2022). Segment detection and pulse compression technology are used to overcome the less output power of SSPA than TWTA. Also, the dual PRF technique is used for velocity dealiasing with the dedicated algorithm. The primary purpose of the TJ-II is to provide a small mass and size, and low-cost 94 GHz MMCR. It can provide reflectivity, mean Doppler velocity and spectral width, and linear depolarization ratio(LDR). The performance metrics of the TJ-II are shown in Tab.1. The peak power of the transmitter is 6 W. The pulse length differs from 1 us to 20 us according to the detection altitude. The detection altitude ranges from 300 m to 15 km, covered by three pulse lengths with an 18.75 m range gate. The pulse repetition time is between 100us and 150us to balance the unambiguous range and Nyquist velocity.

3 Noise level estimation

Similar to other PD radars, after pulse compression and slow-time FFT processing, we can get the Doppler power spectrum of the cloud signal. The Doppler power spectrum reflects the power distribution corresponding to particles with different Doppler velocities. Power spectrum data is related to cloud microphysics and dynamics, which can be obtained by some inversion methods. Also, the Doppler power spectrum is the base of reflectivity, mean Doppler velocity, and spectral width. So power spectrum processing method will directly affect the data quality based on it.

The first is to estimate the noise level. Noise level is the mean noise power in the power spectrum, which is essential for distinguishing signal and noise. The accuracy of the noise level will directly affect the performance of cloud signal detection

https://doi.org/10.5194/amt-2022-302
Preprint. Discussion started: 6 December 2022

Table 1. Performance metrics of the TJ-II MMCR

Frequency	94 GHz
Transmitter type	Solid-state power amplifier
Peak transmitter power	6 W
Antenna type	Singal Cassegrain antenna
Antenna gain	50.8 dBi
Antenna beamwidth	0.45°
Vertical sampling	18.5 m
Pulse width	1.5/5/20 us
Pulse repetition time	100/150 us
FFT points	128/512
Sensitivity	-30 dBZ

and then affect the calculation of the spectral moment. In the early days, the noise level was set to a fixed value(Battan, 1964; Sekhon and Srivastava, 1971). However, the power spectrum will change, and the performance will be poor in different atmospheric backgrounds. In wind profile radar, it is common to treat the mean of the farthest range gate spectrum as the noise level, assuming there is only noise and no signal(Feng et al., 2021). However, in our application, the maximum detection range of TJ-II is 15 km, and some kinds of high clouds exist at this height. So this method is not suitable for TJ-II. Hildebrand and Sekhon (1974) proposed an objective determination method for noise level based on the physical properties of white noise. This method was wildly used in many weather radars. Objective determination starts from the high-power position, searches downwards, and gradually strips the cloud signal until the signal and noise are entirely separated. This method is based on rigorous theory. But in practical application, the amount of calculation is significant, and it is not easy to meet the judgment condition of loop termination. Liu et al. (2014) proposed a method assuming that there is only noise in the power spectrum at a velocity over 8 ms^{-1}, and the mean of these points is the estimated noise level. This method was applied on a Ka-band MMCR with a Nyquist velocity of over 8 ms^{-1}. When it comes to W-band MMCRs, the Nyquist velocity is about one-third of Ka MMCRs with the same Pulse Repetition Time (PRT). For example, in TJ-II, the maximum detection range is 15 km, and the corresponding minimum PRT is 100 us, leading to only about 8 ms^{-1} Nyquist velocity. So LIU's method is incapable of TJ-II because of the narrow Nyquist velocity interval. The velocity dealiasing processing will be discussed in Sect5. Petitdidier et al. (1997) proposed a segment method that divides the power spectrum into multi segments and chooses the minimum mean of these segments as the noise level based on the assumption that cloud signals will not fill the entire power spectrum.

The noise level estimation method in TJ-II is based on the segment method. The following shows the principle of the segment method.

According to the central limit theorem(CLT), the properly normalized sum of independent random variables tends toward a normal distribution. The mean of N random samples with overall mean μ and variance σ^2 follows a normal distribution $N(\mu, \sigma^2/N)$. Meanwhile, the cumulative distribution function(CDF) of the minimum value of M random variables X can be

https://doi.org/10.5194/amt-2022-302
Preprint. Discussion started: 6 December 2022

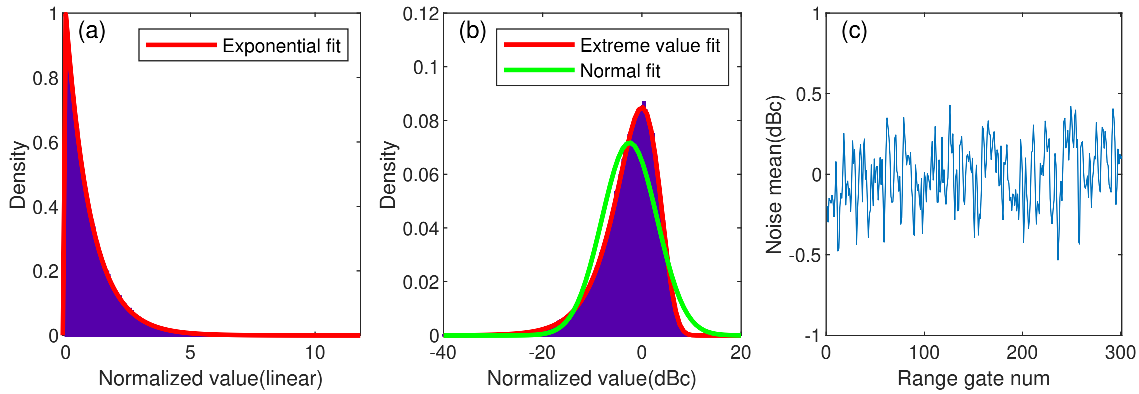

Figure 2. Statistics of noise. (a) linear normalized fit result (b) logarithmic normalized fit result (c) mean noise level of each range gate

given by

$$1-[1-F(x)]^M \tag{1}$$

where $F(x)$ is CDF of X. So CDF of noise level estimated by the segment method can be given by

$$1-[1-\frac{1}{2}erfc(\sqrt{N}\frac{\mu-x}{\sqrt{2}\sigma})]^M \tag{2}$$

From Eq.2, we can find that more points in segment and less segments will result in lower CDF value at the same x value, such as $0.8\mu(-1dBc)$.

Most segment methods divide the spectrum within one range gate. There is a trade-off problem. With a fixed product(FFT points), fewer segments (more points) could decrease the CDF value at a certain threshold but increase the likelihood that cloud signals are present in all segments, leading to an overestimated noise level, especially for signals with wide spectrum width. The narrow Nyquist velocity interval of W-band MMCRs further exacerbates this problem.

Based on the existing observations of TJ-II, we found that the noise in the power spectrum follows an exponential distribution. As shown in Fig.2, a fitting result of linear normalized noise data made by the Matlab Distribution Fitter tool showed a high agreement to an exponential distribution with rate parameter 1. The logarithmic normalized one fitted the extreme value distribution matching the fact that the logarithm of the exponential distribution is the extreme value distribution. So, when it comes to the usual segment method, the noise level with 512 points in a range gate, estimated by eight segments with 64 points, will have about 36% probability of lower than 0.8μ, which we think is a reasonable lower bound of the threshold for noise level estimates. 36% is not acceptable. Even four segments will result in about a 4% probability of lower 0.8μ and may significantly increase the likelihood of cloud signals mixed in all segments in practice due to the narrow Nyquist velocity interval.

A 2-D segment method is proposed to solve the trade-off problem with a single range gate. First, we find the noise in each gate shares almost the same noise level. Fig.2c shows the deviation of the mean noise of each range gate compared with the whole power spectrum mean noise. The deviation of the mean noise is below 1 dB, which allows us to assume that the noise

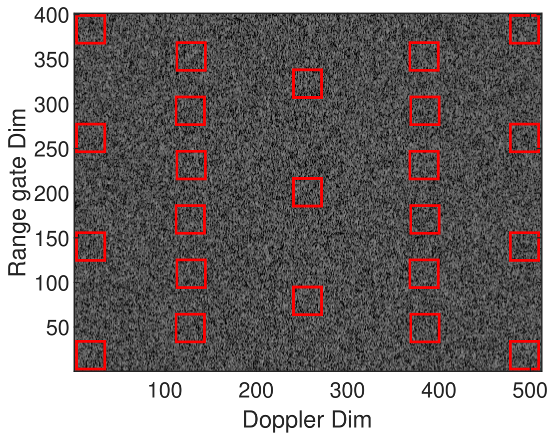

Figure 3. Segments pick example diagram

across the power spectrum shares the same distribution. This assumption makes the 2-D segment method reasonable. Noise from multiple range gates can be used together to estimate the noise level. Points N in the segment can be increased. Second, the number of segments M needs to be limited. If we use the whole power spectrum to divide the segments, the large number of segments M will increase CDF and computation. So we pick some separated segments from the power spectrum. The picking method is shown in Fig.3. **We pick the segments from different velocities and ranges** instead of the fixed velocity and range. For example, picking the segments only at the farthest range gate will result in an overestimation of the noise level in the case of the cloud occurring at the farthest distance, which is possible as the maximum detection range of TJ-II is only 15 km.

Here is the current setting of TJ-II, points in a segment are 961 within a 31 $\times$ 31 window, and the number of segments is 23. So CDF of -1 dBc is about 6.5 $\times 10^{-9}$. Because the segment method uses the minimum mean of segments, inevitably, the noise level will be underestimated. **Compensation is necessary**. The compensation factor is determined by the maximum gradient position of CDF given by Eq.2, which means that the estimated noise level is most likely to fall at this position. The maximum gradient position is about 0.94μ. So the compensation factor F_c is about 1.06.

4 Cloud signal mask method

After getting the noise level, it is time to distinguish between noise and signal. A common method is to use the continuity of velocity spectral width of cloud signals(Shupe et al., 2004; Yuan et al., 2022). Only spectral segment with $N = 2N_h + 1$ continuous bins all over the threshold N_s can be masked as cloud signal. It can be given by Eq.3.

$$M_{1c}(x,y) = \begin{cases} 1, & \sum_{i=-N_h}^{N_h} sign(S(x+i,y) - N_s) = N \\ 0, & else \end{cases} \tag{3}$$

https://doi.org/10.5194/amt-2022-302
Preprint. Discussion started: 6 December 2022

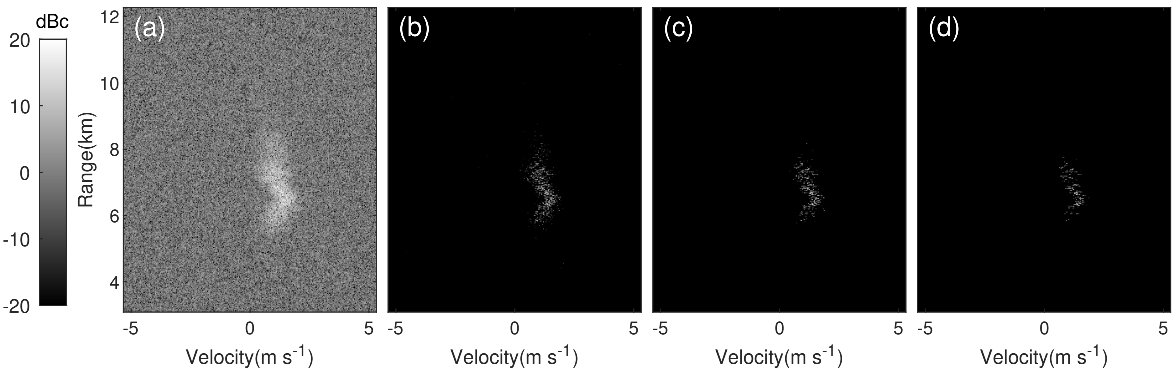

Figure 4. 1-D continuum points method performance with the increasing of N based on actual observation. (a) is the raw Doppler power spectrum; (b), (c), (d) shows the mask result with $N = 3, 5, 7$, respectively. White represents cloud signal, and black represents noise.

$M_{1c}(x, y)$ is the mask result. $S_{i,j}$ is the SNR of power spectrum bins normalized by the noise level, where i and j represent the velocity Dimension and range Dimension, respectively. There is a trade-off on the choice of N between false alarm rate (FAR, noise masked as cloud signal) and missed detection rate (MDR, cloud signal masked as noise). The FAR and MDR of the continuum points method can be given by Eq.4. $F_{noise}(x)$ and $F_{signal}(x)$ represent CDF of noise and signal, respectively.

$$\begin{cases} P_{cFAR} = [1 - F_{noise}(N_s)]^N \\ P_{cMDR} = 1 - [1 - F_{signal}(N_s)]^N \end{cases} \tag{4}$$

The continuum points method shows poor performance for weak cloud signals. As shown in Fig.4 with a threshold $N_s = \mu_n + 2\sigma_n = 3$. This is due to the one-vote veto mechanism of the continuum point method. As long as one value is lower than the threshold, it will be judged as noise and then affect its neighboring signals bins also judged as noise. For weak cloud signals, MDR increases rapidly.

A two-step with 2-D window mask method is proposed benefiting from the high range resolution of TJ-II. The mean of cloud thickness is over 1km, and most are over 0.1 km (Poore et al., 1995; Sun-Mack et al., 2007). The thin cloud usually has very low reflectivity and is, therefore, difficult to be detected. So in TJ-II, the detectable cloud should occupy several range gates, which makes the 2-D window mask method reasonable. Fig.5 shows the schematic flow of our method. First, a pre-mask processing is done based on a central-pixel weighting scheme, as shown in Eq.5. It can also be thought of as smoothing to suppress the noise.

$$M_{2w}(x, y) = \begin{cases} 1, & \sum_{i=-N_h}^{N_h} \sum_{j=-N_h}^{N_h} S(x+i, y+j) \cdot k(i, j) \geq T_s \\ 0, & else \end{cases} \tag{5}$$

$k(i, j)$ is a normalized kernel. It is well known that a larger kernel is more effective in suppressing the noise but blurs the boundary. In TJ-II, a 7 × 7 kernel is used. The type of kernel is also important to better reserve the boundary. The Gaussian

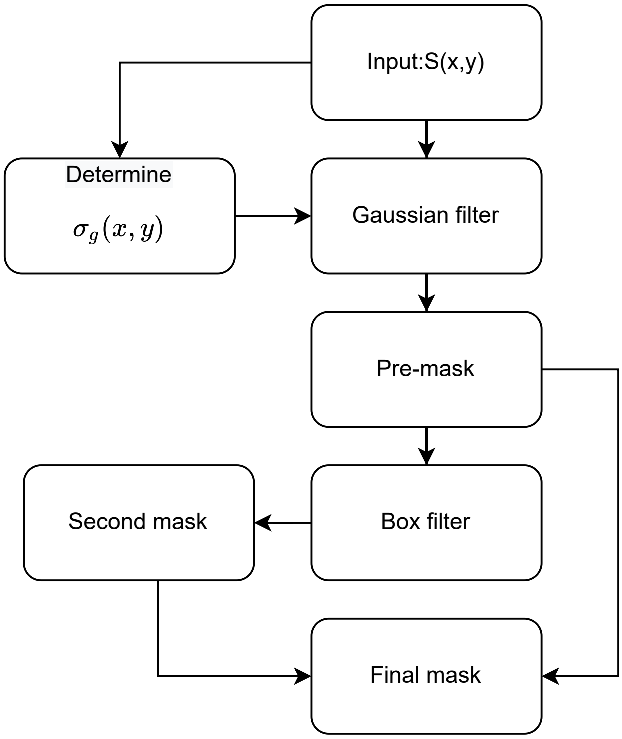

Figure 5. Schematic flow diagram for cloud signal mask method. $S(x,y)$ is the SNR, $\sigma_g(x,y)$ is the standard variance of Gaussian kernel.

kernel, which outputs a "weighted average" of each bin and its neighborhood with the average weighted more towards the value of the central bin, is one of the most common kernels of the noise reduction filter. A 2-D Gaussian distribution kernel can be expressed as

$$G(i,j) = \frac{1}{2\pi\sigma^2}\exp(-\frac{i^2+j^2}{2\sigma^2}) \quad (6)$$

where i and j are the indexes in a kernel window and are 0 for the central bin. σ is the standard deviation of the Gaussian distribution for the window size of the kernel. A Gaussian kernel with variable standard deviation is used in our method. The standard deviation of the Gaussian kernel is determined by the mean value of power spectrum bins in the same window, expressed as

$$\sigma_g(x,y) = \sigma_0 \cdot \max(\frac{T_s}{\mu(x,y)}, \frac{\mu(x,y)}{T_s}) \quad (7)$$

where $\mu(x,y)$ is the mean of the bins in the same window with the central bin at x, y position. σ_0 is the base standard variance. It can represent the deviation from the boundary. The farther from the boundary, the greater the standard variance is used.

A half boundary case was used to evaluate the performance, as shown in Fig.6. Offset is the deviation from the boundary. For the FAR evaluating case shown in Fig.6a, offset 0 means that the central bin is noise and falls at the boundary. The offset

https://doi.org/10.5194/amt-2022-302
Preprint. Discussion started: 6 December 2022

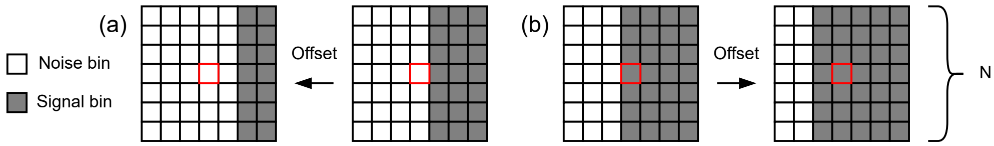

Figure 6. Diagram of half boundary case. (a) noise case for FAR evaluation(b) signal case for MDR evaluation

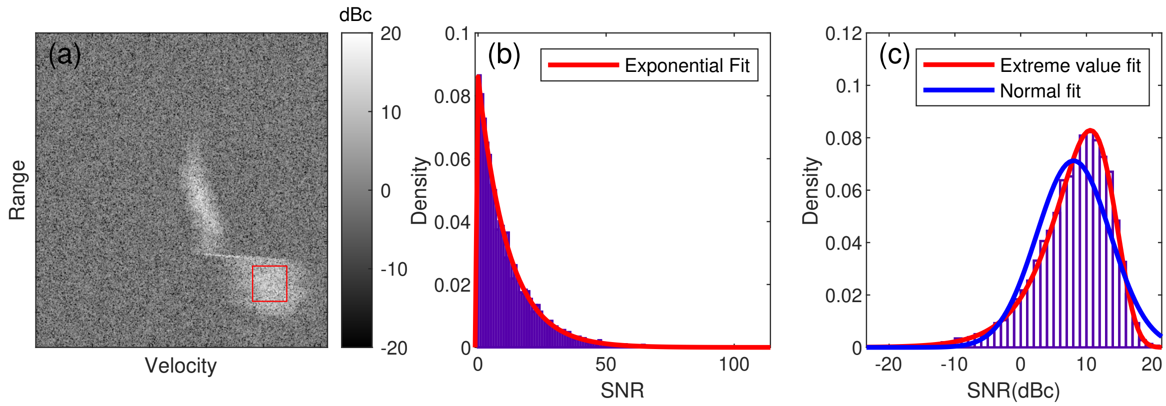

Figure 7. Statistics of manually selected signals. (a) signals picked from the red rectangle area. (b) linear normalized fit result (c) logarithmic normalized fit result

direction is towards the noise area. For the MDR evaluating case shown in Fig.6b, offset 0 means that the central bin is signal and falls at the boundary. The offset direction is towards the signal area.

In our simulation, noise obeyed an exponential distribution with rate parameter 1. The Signal obeyed an exponential distribution with rate parameter 3, which is obtained from $\mu_n + 2\sigma_n$. The assumption of signal distribution was based on our observations. We found the cloud signal manually picked from the TJ-II power spectrum also fitted an exponential distribution, as shown in Fig.7. The performance of our kernel compared with other edge-preserving smoothing filter are shown in Tab.2. The base standard variance σ_0 used in Gaussian, bilateral, and our kernel was 1. The threshold T_s was set to 1.8, a bit lower than 2, the mean of noise and signal mean, which preferred a lower MDR instead of FAR. MDR and FAR of $T_s = 2$ are also shown in Tab.2.

Bilateral, median, Kuwahara, and guided filters all showed unacceptable performance for MDR, even at offset 3, which means there are only signals. Our kernel, Gaussian, and box kernel showed a good balance on both FAR and MDR. Compared with the box kernel, our kernel performed worse for MDR but better FAR at the boundary area. Taking 10 % as the judgment of whether it is easy to blur, our kernel only had two bins, at signal offset 0 and noise offset 0, while the box kernel had three bins, at signal offset 0 and noise offset 0, 1. Compared with the standard Gaussian kernel, our kernel performed better for both MDR and FAR, only except FAR at offset 0.

https://doi.org/10.5194/amt-2022-302
Preprint. Discussion started: 6 December 2022

Table 2. Summary of FAR and MDR using different kernels or filters

Filter type	Performance	OFFSET			
		0	1	2	3
Our kernel	FAR	32.90%	2.11%	0.32%	0.13%
	MDR	19.34%	5.00%	2.37%	1.12%
Gaussian	FAR	29.36%	2.20%	0.91%	1.13%
	MDR	22.14%	7.19%	5.28%	4.60%
Box	FAR	55.20%	18.17%	1.27%	0.00%
	MDR	15.38%	3.36%	0.51%	0.10%
Bilateral	FAR	16.62%	16.33%	16.26%	16.28%
	MDR	44.62%	45.10%	45.17%	44.30%
Median	FAR	0.35%	0.02%	0.00%	0.00%
	MDR	96.24%	81.88%	53.30%	24.53%
Kuwahara	FAR	0.26%	0.14%	0.05%	0.03%
	MDR	87.91%	52.58%	24.51%	10.78%
Guided	FAR	16.63%	16.32%	16.16%	16.02%
	MDR	44.62%	45.06%	45.14%	44.25%
Our kernel	FAR	18.70%	0.64%	0.05%	0.01%
T_s=2	MDR	32.79%	10.81%	6.26%	4.30%

After pre-mask processing, signal blocks are properly masked. There may still be some false detected noise or clutters in the noise area. Moreover, there will be an excessive underestimation of the noise level in a few cases, resulting in much poorer denoising performance. For example, although we have made compensation to the estimated noise level based on the maximum possible interval of 0.94, there is still about a 2 % possibility that the estimated noise level falls at the 0.85 (0.8 to 0.9) interval, leading to increase of SNR based on it. In other words, it lowers the threshold by a scale factor of about 0.9. The FAR of pre-mask processing in the noise area then increases from 0.0009 to 0.005. To further decrease FAR, another mask processing is carried out based on the pre-mask result M_{2w} with a box filter, as shown in Eq.8. It means that if there are over K_sN^2 masked bins in the window, then the center bin is masked as a signal bin. The final mask M_f is the logical conjunction of M_{2n} and M_{2n}, or their product, as shown in Eq.9. K_s is set to 0.35, considering that the round corner case is more common than the square corner. The window size used in this processing can be larger than the one used in pre-mask processing, but K_sN^2 should not exceed the minimum area size wanted to detect. In TJ-II, we want to detect the cloud over 150 m, and the minimum area is about 9 × 9. So the window size should not exceed 15 × 15, calculated by $\sqrt{81/K_s}$. Despite a larger window will increase FAR in the boundary area, these increased false signal bins will not work because the final mask needs both true for

https://doi.org/10.5194/amt-2022-302
Preprint. Discussion started: 6 December 2022

Atmospheric Measurement Techniques Discussions

M_{2w} and M_{2n}.

$$M_{2n}(x,y) = \begin{cases} 1, & \sum_{i=-N_h}^{N_h} \sum_{j=-N_h}^{N_h} M_{2w}(x+i, y+j) \geq K_s N^2 \\ 0, & else \end{cases} \tag{8}$$

$$M_f(x,y) = M_{2w}(x,y) \cdot M_{2n}(x,y) \tag{9}$$

To test the performance of our mask method, we created several signal blocks with size of 50 × 50, 15 × 15, 9 × 9, 7 × 7, 50 × 7 and 50 × 3. The noise was given by an exponential distribution with rate parameter 1. The Signal was given by an exponential distribution with rate parameter 3. Fig.8 shows the result after pre-mask and final mask processing. For pre-mask processing, it could properly mask out signal blocks larger than the pre-mask window. For signal blocks like 50 × 3 with one dimension too small, there was a large MDR. For final mask processing, the false detected noises in the full noise area by pre-mask processing were all removed. For the signal blocks larger than the second mask window, the final mask had few effects on them. For the small signal block between the second mask processing and pre-mask processing window, like the 9 × 9 block, its boundary was narrowed. For the 7 × 7 signal block, which is lower than the set minimum detectable size 9 × 9, it was completely erased. 50 × 7 signal block was well reserved because of the expansion of one dimension, while 50 × 3 signal block was removed because of the much smaller size of one dimension.

There is a trade-off in both window size and threshold selection. For weaker cloud detection, the threshold of pre-mask processing needs to be lower, and the window size of second mask processing needs to be increased to account for increased FAR. But the sensitivity to small signal blocks will be decreased. These parameters need to be fine-tuned based on demands and long-term observations.

5 Velocity dealiasing with dual PRF technique

Before calculating the base datum from the power spectrum data, one more processing is necessary for MMCR. That is the velocity dealiasing. Velocity aliasing, also called velocity folding, is a common phenomenon for cloud radar, especially for MMCRs whose short wavelength λ leads to narrow Nyquist velocity interval according to Eq.10. So velocity dealiasing is critical for cloud radar data quality control.

$$V_m = \frac{\lambda PRF}{4} \tag{10}$$

For most weather radar, velocity dealiasing is done at the base datum stage. There are many studies on dealiasing the velocity at the base datum stage(Ray and Ziegler, 1977; Merritt, 1984; Gong et al., 2003; James and Houze, 2001). The dealiased velocity V_f is equal to $V_i \pm 2nV_{max}$, where the correctness of the initial velocity V_i is the key. Unlike common weather radar, velocity dealiasing of vertical sensing MMCRs must be done at the power spectrum stage to ensure the accuracy of V_i.

https://doi.org/10.5194/amt-2022-302
Preprint. Discussion started: 6 December 2022

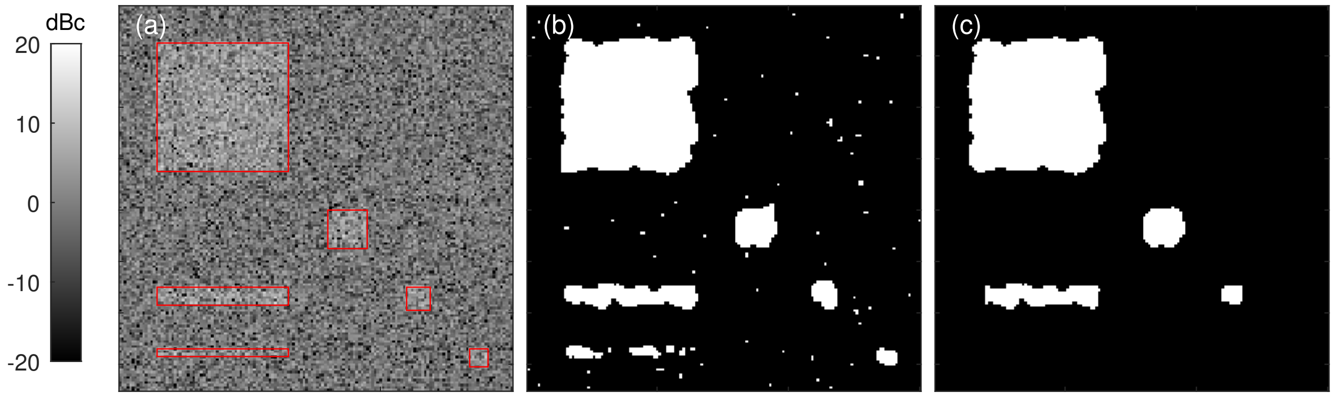

Figure 8. Cloud signal mask processing simulation with different block sizes. (a) signals with noise (b) pre-mask processing result (c) final mask processing result

As shown in Fig.10(c1), there is a clear half-folded state that signal bins fall at both maximum positive and negative velocities. If velocity dealiasing is not done at the power spectrum stage, then V_i will have a significant error and affect the dealiased velocity V_f obtained by $V_i \pm 2nV_{max}$. Zheng et al. (2016) takes an iterative algorithm that assumes no velocity aliasing at the cloud top and then iterates down to the bottom. It may fail in extreme weather conditions where the assumption does not hold. Also, if a dealiasing error or outlier occurs at one range gate, the error will be propagated to all subsequent range gates. In TJ-II, a dual PRF technique was used to extend the actual Nyquist velocity interval. By using a high and a low PRF with Nyquist velocities of and V_{mh} and V_{ml}, respectively, the new extended Nyquist velocity becomes (Dazhang et al. 1984)

$$V_{mn} = \frac{V_{mh}V_{ml}}{V_{mh} - V_{ml}} \tag{11}$$

A common practice for choosing the high and low PRFs is the following way:

$$\frac{V_{mh}}{V_{ml}} = \frac{PRF_h}{PRF_l} = \frac{PRT_l}{PRT_h} = \frac{N+1}{N} \tag{12}$$

For a fixed value of the high PRF, the choice of N involves a trade-off between the maximum extension of the Nyquist velocity V_{mn} and ΔV_{max}. Dual PRF dealiasing errors will occur if the difference between the true velocities, caused by noise, etc., exceeds ΔV_{max} (Joe and May, 2003; Altube et al., 2017).

$$\Delta V_{max} = \frac{V_{mn}}{N(N+1)} = \frac{V_{mh}}{N+1} \tag{13}$$

In TJ-II, the high PRF is limited to 10kHz (equivalent to 100us PRT) due to the maximum detection range of $15km$. So the V_{mh} is no more than about $8m/s$. $N = 2$ is used considering the vertical velocity of the cloud will not be so large and for a larger ΔV_{max}.

The common dual PRF velocity estimate method in Eq.14 shows a poor accuracy that its standard deviation will be amplified(Holleman and Beekhuis, 2003). So it is merely used to indicate to which Nyquist interval the original (folded) velocity

https://doi.org/10.5194/amt-2022-302
Preprint. Discussion started: 6 December 2022

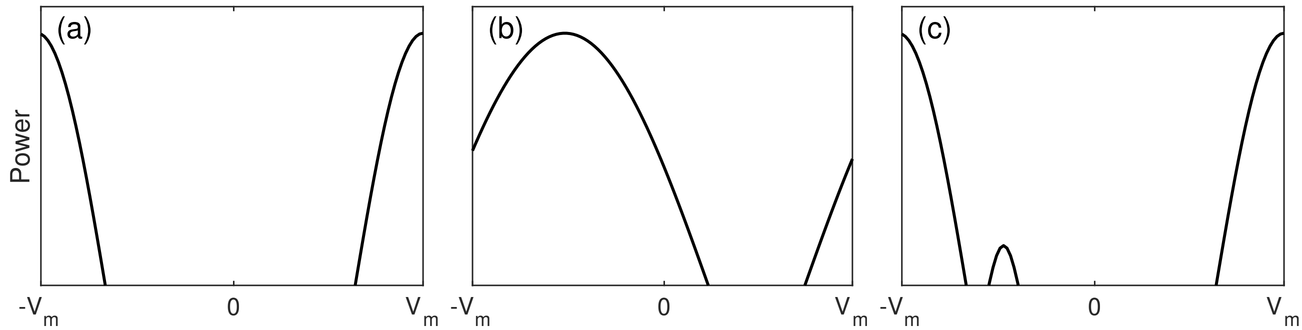

Figure 9. Some cases of half-folded state. (a)normal case (b)case with ultra-wide spectral width (c)case with sub peak

estimates belong.

$$V_{lh} = (N+1)V_l - NV_h \tag{14}$$

where V_l and V_h are the original raw velocity estimate using the low and high PRF, respectively. When V_{lh} falls out of the primary Nyquist velocity interval $\pm V_{mn}$, it needs to be folded back into the primary interval by $\pm 2V_{mn}$.

A correct raw velocity estimate is the base of dealiasing. For some weather radars, the velocity spectral width is much smaller than the velocity, which can be handled like a point target. But for vertical sensing MMCRs, the spectral width and velocity are similar. For a full-folded case, it has no effect. But the case called half-folded or partial folded, shown in Fig.9, will severely affect the correctness of the raw velocity estimate because of crossing 2 Nyquist velocity interval. For example, in Fig.9a case, velocity without processing is $0 \pm 2nV_m$ while the true velocity is $V_m \pm 2nV_m$. There must be a preliminary dealiasing before applying the dual PRF technique. Both five bins closed to the maximum positive and negative velocity are used to distinguish folded type. If there are at least three masked bins on both sides, then it is considered as half-folded, otherwise full-folded(or non-folded). Multi bins are used to exclude the effect of false detected noise bins.

For half-folded, the dividing line of two parts needs to be determined. The easiest way is to use the zero point as a dividing line. But it will fail for the case shown in Fig.9b. The median of noise bins is taken as the dividing line instead of the middle point of signal bins endpoints used by Zheng et al. (2016) to avoid the case shown in Fig.9c, that there is a sub-peak and the four endpoints complicating endpoints selection. Then we need to fold one part back into another. There is no difference between folding negative to positive and positive to negative by the following processing. In TJ-II, the negative part is folded back into the positive part, and the new defolded mean velocity is calculated. If the new defolded mean velocity is over the primary Nyquist velocity V_m, it needs to be folded back into the primary Nyquist interval by $-2V_m$ as the final raw velocity estimate. Now we can use the dual PRF technique.

To estimate the final Nyquist interval, considering the N in TJ-II is only two, the exhaustive method is used instead of Eq.14, where occasionally the deviation of the primary dual PRF velocity estimate will be so large that the original folded velocity will be assigned to an incorrect Nyquist interval(Holleman and Beekhuis, 2003). By exhausting all interval combinations, the

https://doi.org/10.5194/amt-2022-302
Preprint. Discussion started: 6 December 2022

Atmospheric Measurement Techniques Discussions

Table 3. Interval combination

Nyquist interval	Velocity interval		Nyquist interval
PRF_h		PRF_l	
1	(8,24)	(5.33,16)	1
0	(-8,8)	(5.33,16)	1
		(-5.33,5.33)	0
		(-16,-5.33)	-1
-1	(-24,-8)	(-16,-5.33)	-1

interval combination with the minimum difference is taken as the estimated interval. Considering the coverage of each interval, the combination can be simplified as shown in Tab.3

6 Application to TJ-II observations

Our Doppler power spectrum processing method was applied to the TJ-II raw power spectrum data. Fig.10 shows three typical case. For Fig.10a case, the cloud signal block was well detected, and the noise was removed. There were some miss detections at the top of the signal block. For Fig.10b case, there were already some miss detections at the pre-mask stage and more after final mask processing. The mean SNR of detected signals was about 2.3, which is lower than our preset threshold. For Fig.10c, there were significantly more mismarked noises by pre-mask processing. Because the estimated noise level, which was already compensated, was about 0.84 of the manually picked noise level by calculating the mean of the top 50 range gates with over $2.5\ \times 10^4$ points. The underestimated noise level led to an equivalent drop in the threshold T_s used in pre-mask processing, resulting in a larger increase of FAR. But the final mask processing removed all these noises benefiting from a larger window than the one used in pre-marking processing.

One example of velocity dealiasing is shown in Fig.11 to demonstrate the necessity of pre-defolding processing in MMCRs. This example was observed just before rain. There was a clear velocity aliasing in Fig.11a1 with a half-folded state. There was a sudden bend when the half-folded state occurred. In the distance segment with a half-folded state, the raw mean velocity line without pre-defolding processing had obvious larger burrs, as shown in Fig.11b1. There were some jumps in the mean velocity line with pre-defolding processing because the velocity exceeding the primary Nyquist interval was folded back to the primary Nyquist interval in the processing for the convenience of dual PRF processing. The final dealiased result is shown in Fig.11b2. Of course, the incorrect raw mean velocity led to the incorrect final mean velocity.

Our method was compared to the Jinming Ge's method(Ge et al., 2017) to assess the cloud mask performance by applied to the one-day example of TJ-II observed on 17 November 2021 at Nanjing, as shown in Fig.12. Jinming Ge's method masks the cloud at the base datum stage, which means post-processing, while our method masks the cloud at the Doppler power spectrum stage. Fig.11a is the raw reflectivity without any processing. The unit is dBm because the calibration of the TJ-II has

https://doi.org/10.5194/amt-2022-302
Preprint. Discussion started: 6 December 2022

Atmospheric Measurement Techniques Discussions

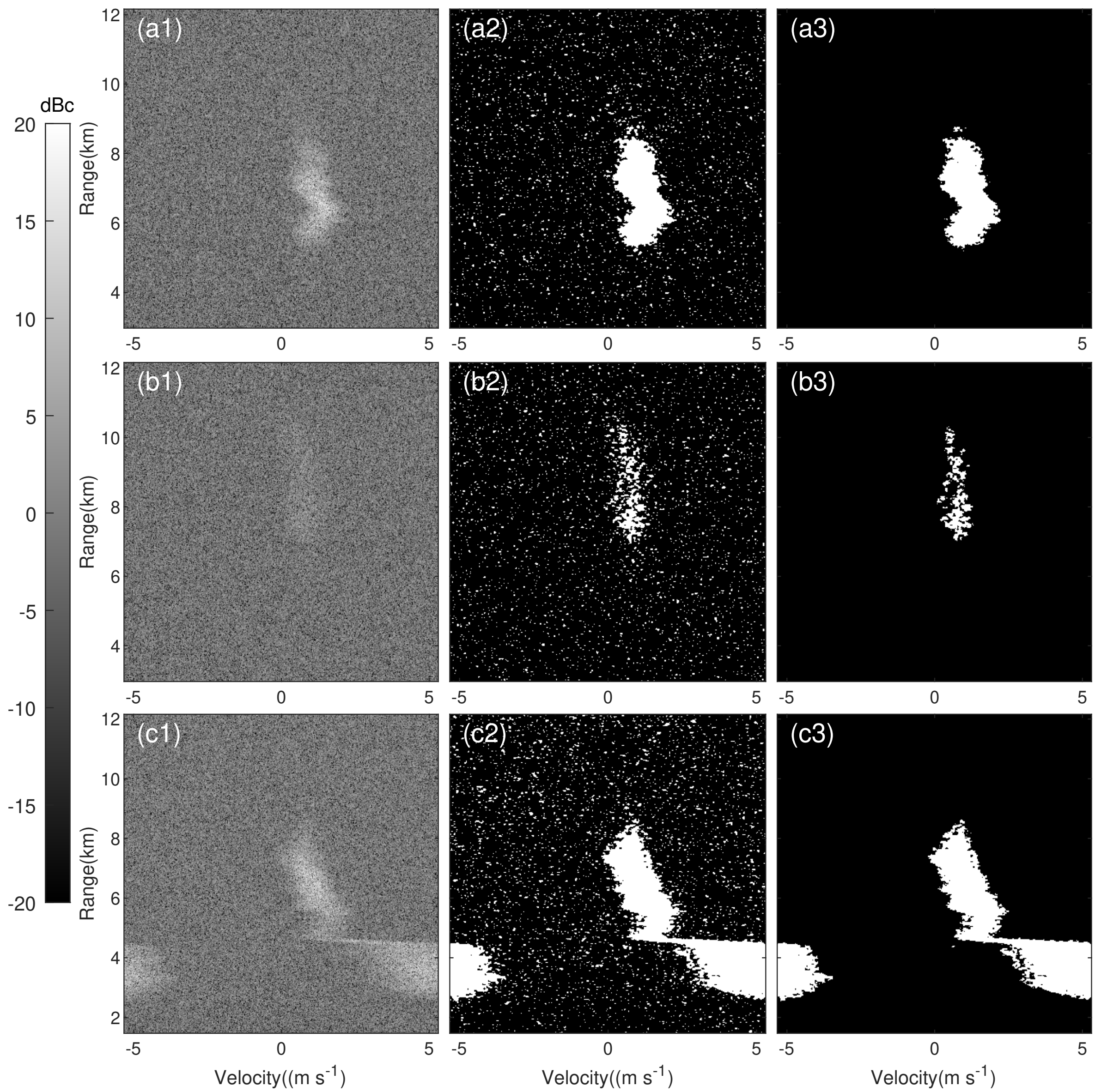

Figure 10. Three cases of power spectrum from TJ-II observation. (a) is the common case, (b) is the case with weak signals, and (c) is the case with an underestimated noise level. (1) is the raw power spectrum, (2) is the pre-mask result and (3) is the final mask result

https://doi.org/10.5194/amt-2022-302
Preprint. Discussion started: 6 December 2022

Atmospheric Measurement Techniques Discussions

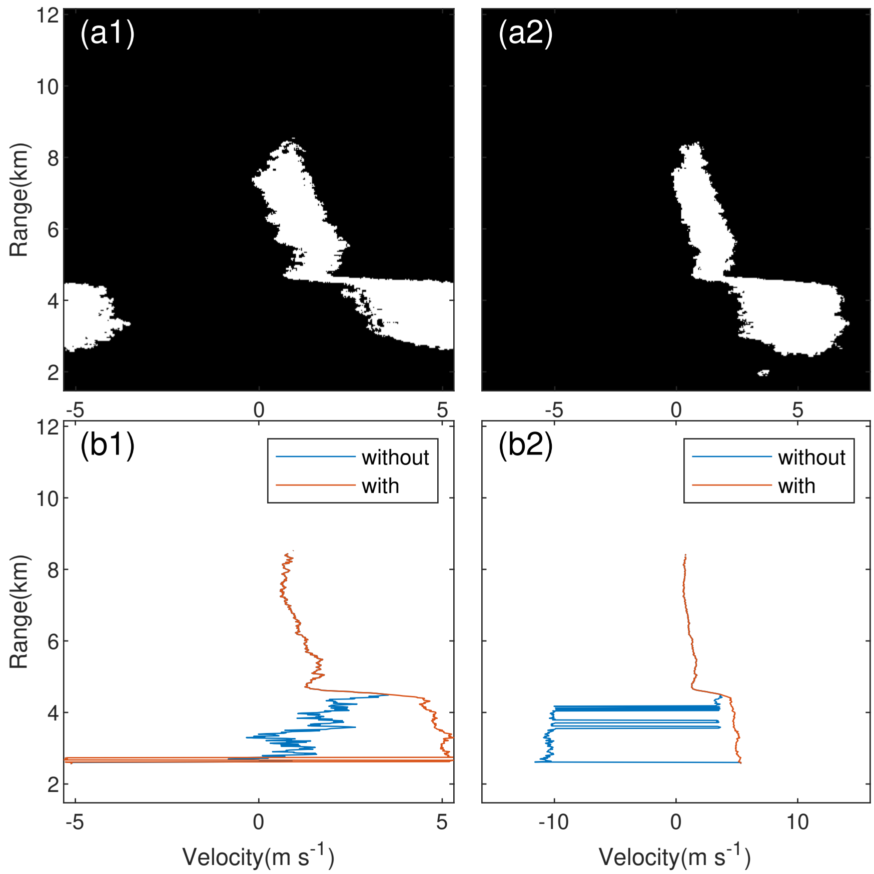

Figure 11. One example with a half-folded state. (a1) and (a2) is the mask result by cloud signal mask processing with PRT 150us and 100us, respectively. (b1) is the raw mean velocity of (a1) with and without pre-defolding processing. (b2) is the final dealiased velocity with and without pre-defolding processing

not been completed. Fig.11b is the mask by our method processing at the Doppler power spectrum stage as pre-processing, and Fig.11c is the mask by Jinming Ge's method processing at the base datum stage as post-processing. Fig.11d shows the comparison between the two methods. Yellow represents only masked by our method. Blue represents only masked by Jinming Ge's method. Gray represents both or neither masked by both methods. Yellow tended to surround blue, especially for the cloud base, which means that our method performs better for cloud base detection. For the cloud top, although yellow still showed a tendency to wrap blue, there was a marked increase in blue. These missed masks, by our method, meant a drop in performance at the cloud top. For the area around about 9 km and 10 o'clock, both our method and Jinming Ge's method showed poor performance for these extremely weak signals. For the free space, there was much less yellow than blue. Our method offered a better FAR than Jinming Ge's method.

https://doi.org/10.5194/amt-2022-302
Preprint. Discussion started: 6 December 2022

Atmospheric Measurement Techniques
Discussions

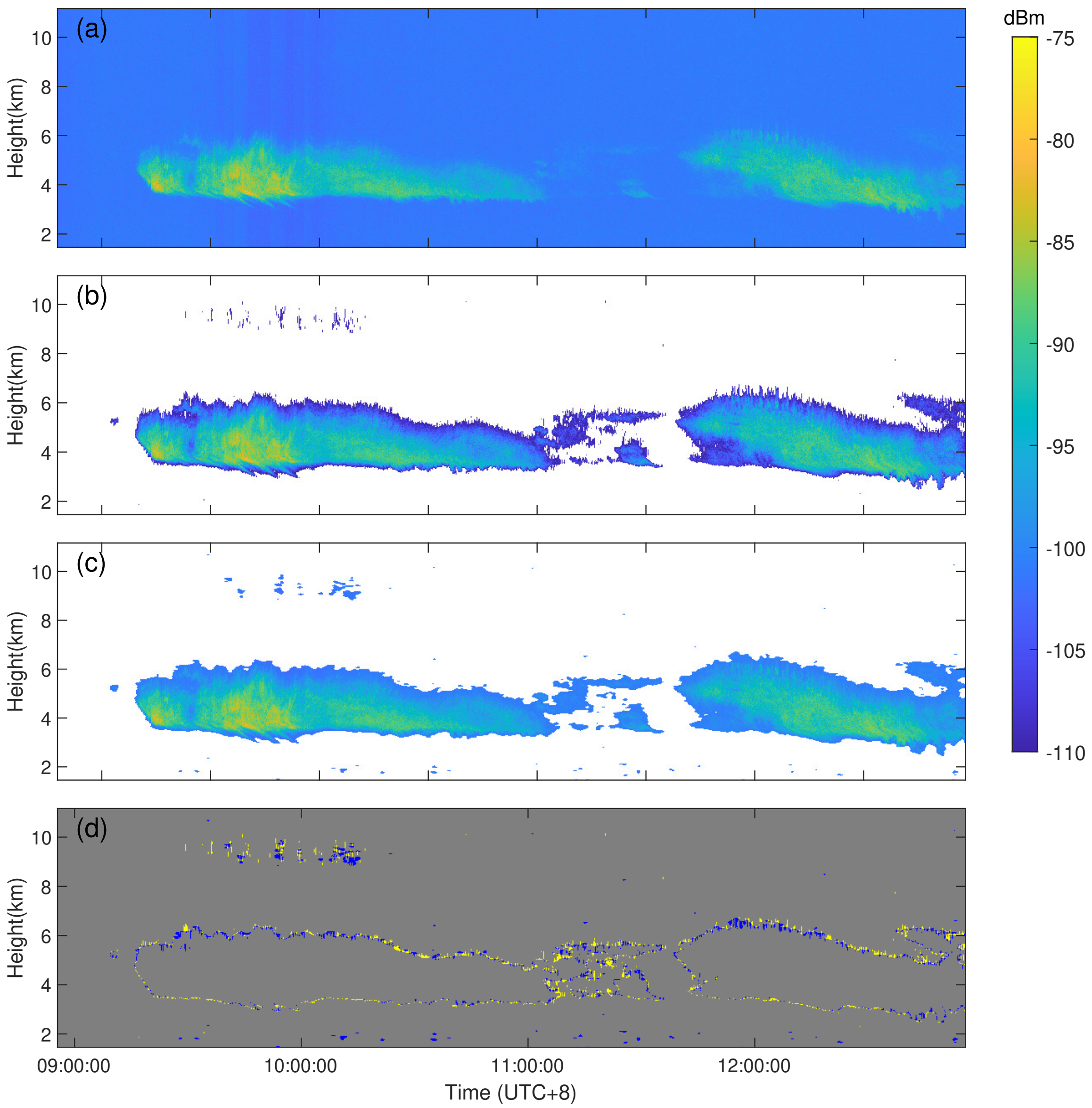

Figure 12. One-day example of TJ-II observed on 17 November 2021. (a) raw reflectivity; (b) cloud derived by our method; (c) cloud derived from raw reflectivity by Jinming Ge's method; (d) comparison of cloud mask results between the two methods. Yellow represents only masked by our method, blue represents only masked by Jinming Ge's method, and gray represents both or neither masked by both methods.

https://doi.org/10.5194/amt-2022-302
Preprint. Discussion started: 6 December 2022

Atmospheric Measurement Techniques
Discussions

7 Summary and dicussion

MMCR is an excellent tool for cloud sensing. Vertical sensing MMCR has unique characteristics, which makes its signal processing method different from traditional weather radar. A new MMCR called TJ-II with a single antenna and SSPA was developed. A set of Doppler power spectrum processing methods for this MMCR is proposed based on its characteristics. It includes three aspects: noise level estimation, cloud signal mask, and velocity dealiasing. Noise level is estimated by an improved segment method to cope with the relatively narrow detection range and Nyquist velocity interval of the TJ-II. A 2-D segment is used to increase the points and a small number of separated segments to reduce the total number of segments while reducing the risk of including signals. A two-step cloud signal mask method was proposed benefiting from the high spatial and temporal resolution. A standard variance adaptive 2-D Gaussian weighting kernel is used in pre-mask processing to ensure high performance in identifying cloud signals and their edges, and the following step uses a 2-D box filter to remove the noise. The dual PRF technique is used in TJ-II to expand the actual Nyquist velocity interval. A pre-dealiasing processing is performed to the masked power spectrum before the raw velocity is used in dual PRF processing. The example shown in Fig.11 demonstrated its necessity. These methods are proposed for better data quality, benefiting from or limited by the characteristics of vertical sensing MMCRs. In particular, some small probability cases have been considered. Our method exhibits comparable performance compared to Jinming Ge's method, which represents a post-processing method for MMCR. Considering the particular half-folded velocity aliasing case in vertical sensing MMCRs, pre-processing at the Doppler power spectrum stage will be preferred. With long-term observations in the future, the parameters used in our method have room for optimization. Along with the development of TJ-II, some matching post-processing methods are also under study for better total performance. The above signal processing methods are proposed for better data quality, benefiting from or limited by the characteristics of vertical sensing MMCRs. In particular, some small probability cases have been considered. High-quality cloud data will be of great help to cloud research.

Code and data availability. Data and code related to this article are available upon request to the corresponding author.

Author contributions. Hai Lin and Junxiang Ge planned the research. HAI LIN designed the algorithm and wrote the paper under the guidance of Ge. Hai Lin, Jie Wang, and Zhenhua Chen were in charge of radar hardware and observation experiments. Junxiang Ge was in charge of the whole project.

Competing interests. The authors declare that they have no conflict of interest.

Acknowledgements. This work was supported in part by the National Natural Science Foundation of China under Grant 61671249, and in part by the Jiangsu Innovation and Entrepreneurship Group Talents Plan.

https://doi.org/10.5194/amt-2022-302
Preprint. Discussion started: 6 December 2022

References

Altube, P., Bech, J., Argemí, O., Rigo, T., Pineda, N., Collis, S., and Helmus, J.: Correction of dual-PRF Doppler velocity outliers in the presence of aliasing, Journal of Atmospheric and Oceanic Technology, 34, 1529–1543, https://doi.org/10.1175/JTECH-D-16-0065.1, 2017.

Ansmann, A. and Müller, D.: Lidar and atmospheric aerosol particles, in: Lidar, pp. 105–141, Springer, https://doi.org/10.1007/0-387-25101-4_4, 2005.

Arking, A.: The radiative effects of clouds and their impact on climate, Bulletin of the American Meteorological Society, 72, 795–814, https://doi.org/10.1175/1520-0477(1991)072<0795:TREOCA>2.0.CO;2, 1991.

Baars, H., Ansmann, A., Engelmann, R., and Althausen, D.: Continuous monitoring of the boundary-layer top with lidar, Atmospheric chemistry and Physics, 8, 7281–7296, https://doi.org/10.5194/acp-8-7281-2008, 2008.

Baker, M. B. and Peter, T.: Small-scale cloud processes and climate, Nature, 451, 299–300, https://doi.org/10.1038/nature06594, 2008.

Battan, L. J.: Some observations of vertical velocities and precipitation sizes in a thunderstorm, Journal of Applied Meteorology (1962-1982), pp. 415–420, https://doi.org/10.1175/1520-0450(1964)003<0415:SOOVVA>2.0.CO;2, 1964.

Bony, S., Stevens, B., Frierson, D. M., Jakob, C., Kageyama, M., Pincus, R., Shepherd, T. G., Sherwood, S. C., Siebesma, A. P., Sobel, A. H., et al.: Clouds, circulation and climate sensitivity, Nature Geoscience, 8, 261–268, https://doi.org/10.1038/NGEO2398, 2015.

Chandra, A., Zhang, C., Kollias, P., Matrosov, S., and Szyrmer, W.: Automated rain rate estimates using the Ka-band ARM zenith radar (KAZR), Atmospheric Measurement Techniques, 8, 3685–3699, https://doi.org/10.5194/amt-8-3685-2015, 2015.

Collins, W., Colman, R., Haywood, J., Manning, M. R., and Mote, P.: The physical science behind climate change, Scientific American, 297, 64–73, https://doi.org/10.1038/scientificamerican0807-64, 2007.

Danne, O., Quante, M., Milferstädt, D., Lemke, H., and Raschke, E.: Relationships between Doppler spectral moments within large-scale cirro-and altostratus cloud fields observed by a ground-based 95-GHz cloud radar, Journal of Applied Meteorology, 38, 175–189, https://doi.org/10.1175/1520-0450(1999)038<0175:RBDSMW>2.0.CO;2, 1999.

Delanoë, J., Protat, A., Vinson, J.-P., Brett, W., Caudoux, C., Bertrand, F., Du Châtelet, J. P., Hallali, R., Barthes, L., Haeffelin, M., et al.: BASTA: A 95-GHz FMCW Doppler radar for cloud and fog studies, Journal of Atmospheric and Oceanic Technology, 33, 1023–1038, https://doi.org/10.1175/JTECH-D-15-0104.1, 2016.

Feng, L., Zheng, R., Hongyan, W., and Runsheng, G.: A calibration method of wind profile radar echo intensity with Doppler velocity spectrum, Journal of Applied Meteorological Science, 32, 315–331, https://doi.org/10.11898/1001-7313.20210305, 2021.

Ge, J., Zhu, Z., Zheng, C., Xie, H., Zhou, T., Huang, J., and Fu, Q.: An improved hydrometeor detection method for millimeter-wavelength cloud radar, Atmospheric Chemistry and Physics, 17, 9035–9047, https://doi.org/10.5194/acp-17-9035-2017, 2017.

Gong, J., Wang, L. L., and Xu, Q.: A three-step dealiasing method for Doppler velocity data quality control, Journal of Atmospheric and Oceanic Technology, 20, 1738–1748, https://doi.org/10.1175/1520-0426(2003)020<1738:ATDMFD>2.0.CO;2, 2003.

Hildebrand, P. H. and Sekhon, R.: Objective determination of the noise level in Doppler spectra, Journal of Applied Meteorology (1962-1982), pp. 808–811, https://doi.org/10.1175/1520-0450(1974)013<0808:ODOTNL>2.0.CO;2, 1974.

Hogan, R. J., Bouniol, D., Ladd, D. N., O'Connor, E. J., and Illingworth, A. J.: Absolute calibration of 94/95-GHz radars using rain, Journal of Atmospheric and Oceanic Technology, 20, 572–580, https://doi.org/10.1175/1520-0426(2003)20<572:ACOGRU>2.0.CO;2, 2003.

Holleman, I. and Beekhuis, H.: Analysis and correction of dual PRF velocity data, Journal of Atmospheric and Oceanic Technology, 20, 443–453, https://doi.org/10.1175/1520-0426(2003)20<443:AACODP>2.0.CO;2, 2003.

Huggard, P., Oldfield, M., Moyna, B., Ellison, B., Matheson, D., Bennett, A., Gaffard, C., Oakley, T., and Nash, J.: 94 GHz FMCW cloud radar, in: Millimetre Wave and Terahertz Sensors and Technology, vol. 7117, pp. 16–21, SPIE, https://doi.org/10.1117/12.800347, 2008.

Im, E., Wu, C., and Durden, S. L.: Cloud profiling radar for the CloudSat mission, in: IEEE International Radar Conference, 2005., pp. 483–486, IEEE, https://doi.org/10.1109/RADAR.2005.1435874, 2005.

James, C. N. and Houze, R. A.: A real-time four-dimensional Doppler dealiasing scheme, Journal of Atmospheric and Oceanic Technology, 18, 1674–1683, https://doi.org/10.1175/1520-0426(2001)018<1674:ARTFDD>2.0.CO;2, 2001.

Joe, P. and May, P.: Correction of dual PRF velocity errors for operational Doppler weather radars, Journal of Atmospheric and Oceanic Technology, 20, 429–442, https://doi.org/10.1175/1520-0426(2003)20<429:CODPVE>2.0.CO;2, 2003.

Kim, S.-W., Chung, E.-S., Yoon, S.-C., Sohn, B.-J., and Sugimoto, N.: Intercomparisons of cloud-top and cloud-base heights from ground-based Lidar, CloudSat and CALIPSO measurements, International journal of remote sensing, 32, 1179–1197, https://doi.org/10.1080/01431160903527439, 2011.

Kollias, P., Clothiaux, E., Miller, M., Albrecht, B., Stephens, G., and Ackerman, T.: Millimeter-wavelength radars: New frontier in atmospheric cloud and precipitation research, Bulletin of the American Meteorological Society, 88, 1608–1624, https://doi.org/10.1175/BAMS-88-10-1608, 2007.

Kropfli, R., Matrosov, S., Uttal, T., Orr, B., Frisch, A., Clark, K., Bartram, B., Reinking, R., Snider, J., and Martner, B.: Cloud physics studies with 8 mm wavelength radar, Atmospheric Research, 35, 299–313, https://doi.org/10.1016/0169-8095(94)00025-9, 1995.

Kumjian, M. R.: Weather radars, in: Remote sensing of clouds and precipitation, pp. 15–63, Springer, https://doi.org/10.1007/978-3-319-72583-3_2, 2018.

Lamb, D. and Verlinde, J.: Physics and chemistry of clouds, Cambridge University Press, https://doi.org/10.1017/CBO9780511976377, 2011.

Lhermitte, R.: A 94-GHz Doppler radar for cloud observations, Journal of Atmospheric and Oceanic Technology, 4, 36–48, https://doi.org/10.1175/1520-0426(1987)004<0036:AGDRFC>2.0.CO;2, 1987a.

Lhermitte, R. M.: Small cumuli observed with a 3 mm wavelength Doppler radar, Geophysical research letters, 14, 707–710, https://doi.org/10.1029/GL014i007p00707, 1987b.

Liu, L., Xie, L., and Cui, Z.: Examination and application of Doppler spectral density data in drop size distribution retrieval in weak precipitation by cloud radar, Chin. J. Atmos. Sci, 38, 223–236, https://doi.org/10.3878/j.issn.1006-9895.2013.12207, 2014.

McGill, M., Hlavka, D., Hart, W., Scott, V. S., Spinhirne, J., and Schmid, B.: Cloud physics lidar: Instrument description and initial measurement results, Applied Optics, 41, 3725–3734, https://doi.org/10.1364/AO.41.003725, 2002.

Merritt, M.: Automatic velocity de-aliasing for real-time applications((in radar wind velocity measurement)), in: Conference on Radar Meteorology, 22 nd, Zurich, Switzerland, pp. 528–533, 1984.

Müller, D., Ansmann, A., Mattis, I., Tesche, M., Wandinger, U., Althausen, D., and Pisani, G.: Aerosol-type-dependent lidar ratios observed with Raman lidar, Journal of Geophysical Research: Atmospheres, 112, https://doi.org/10.1029/2006JD008292, 2007.

Muller, J.-P. and Fischer, J.: The EU-CLOUDMAP project: Cirrus and contrail cloud-top maps from satellites for weather forecasting climate change analysis, International Journal of Remote Sensing, 28, 1915–1919, https://doi.org/10.1080/01431160600641913, 2007.

Petitdidier, M., Sy, A., Garrouste, A., and Delcourt, J.: Statistical characteristics of the noise power spectral density in UHF and VHF wind profilers, Radio Science, 32, 1229–1247, https://doi.org/10.1029/97RS00250, 1997.

Poore, K. D., Wang, J., and Rossow, W. B.: Cloud layer thicknesses from a combination of surface and upper-air observations, Journal of Climate, 8, 550–568, https://doi.org/10.1175/1520-0442(1995)008<0550:CLTFAC>2.0.CO;2, 1995.

https://doi.org/10.5194/amt-2022-302
Preprint. Discussion started: 6 December 2022

Atmospheric Measurement Techniques
Discussions

Ran, Y., Wang, H., Tian, L., Wu, J., and Li, X.: Precipitation cloud identification based on faster-RCNN for Doppler weather radar, EURASIP Journal on Wireless Communications and Networking, 2021, 1–20, https://doi.org/10.1186/s13638-021-01896-5, 2021.

Ray, P. S. and Ziegler, C.: De-aliasing first-moment Doppler estimates, Journal of Applied Meteorology and Climatology, 16, 563–564, https://doi.org/10.1175/1520-0450(1977)016<0563:DAFMDE>2.0.CO;2, 1977.

Rosenfeld, D.: Aerosol-cloud interactions control of earth radiation and latent heat release budgets, Solar Variability and Planetary Climates, pp. 149–157, https://doi.org/10.1007/978-0-387-48341-2_12, 2006.

Sekhon, R. S. and Srivastava, R.: Doppler radar observations of drop-size distributions in a thunderstorm, Journal of the Atmospheric Sciences, 28, 983–994, https://doi.org/10.1175/1520-0469(1971)028<0983:DROODS>2.0.CO;2, 1971.

Shupe, M. D., Kollias, P., Matrosov, S. Y., and Schneider, T. L.: Deriving mixed-phase cloud properties from Doppler radar spectra, Journal of Atmospheric and Oceanic Technology, 21, 660–670, https://doi.org/10.1175/1520-0426(2004)021<0660:DMCPFD>2.0.CO;2, 2004.

Solomon, S., Qin, D., Manning, M., Averyt, K., and Marquis, M.: Climate change 2007-the physical science basis: Working group I contribution to the fourth assessment report of the IPCC, vol. 4, Cambridge university press, https://www.ipcc.ch/report/ar4/wg1/, 2007.

Stephens, G. L., Vane, D. G., Boain, R. J., Mace, G. G., Sassen, K., Wang, Z., Illingworth, A. J., O'connor, E. J., Rossow, W. B., Durden, S. L., et al.: The CloudSat mission and the A-Train: A new dimension of space-based observations of clouds and precipitation, Bulletin of the American Meteorological Society, 83, 1771–1790, https://doi.org/10.1175/BAMS-83-12-1771, 2002.

Sun-Mack, S., Minnis, P., Chen, Y., Gibson, S., Yi, Y., Trepte, Q., Wielicki, B., Kato, S., Winker, D., Stephens, G., et al.: Integrated cloud-aerosol-radiation product using CERES, MODIS, CALIPSO, and CloudSat data, in: Remote Sensing of Clouds and the Atmosphere XII, vol. 6745, pp. 277–287, SPIE, https://doi.org/10.1117/12.737903, 2007.

Takano, T., Nakanishi, Y., and Takamura, T.: High resolution FMCW Doppler radar FALCON-I for W-band meteorological observations, in: 2012 15 International Symposium on Antenna Technology and Applied Electromagnetics, pp. 1–4, IEEE, https://doi.org/10.1109/ANTEM.2012.6262419, 2012.

Verlinde, J., Rambukkange, M. P., Clothiaux, E. E., McFarquhar, G. M., and Eloranta, E. W.: Arctic multilayered, mixed-phase cloud processes revealed in millimeter-wave cloud radar Doppler spectra, Journal of Geophysical Research: Atmospheres, 118, 13–199, https://doi.org/10.1002/2013JD020183, 2013.

Wang, J., Lin, H., Yang, F., Xu, G., and Ge, J.: Design of 94GHz Dual-Polarization Antenna Fed by Diagonal Horn for Cloud Radars, IEEE Access, 10, 22 480–22 486, https://doi.org/10.1109/ACCESS.2022.3154483, 2022.

Wu, J., Wei, M., Hang, X., Zhou, J., Zhang, P., and Li, N.: The first observed cloud echoes and microphysical parameter retrievals by China's 94-GHz cloud radar, Journal of Meteorological Research, 28, 430–443, https://doi.org/10.1007/s13351-014-3083-x, 2014.

Yan, Y., Liu, Y., Liu, X., and Wang, X.: Effects of Cloud Microphysics on the Vertical Structures of Cloud Radiative Effects over the Tibetan Plateau and the Arctic, Remote Sensing, 13, 2651, https://doi.org/10.3390/rs13142651, 2021.

Yuan, Y., Di, H., Liu, Y., Yang, T., Li, Q., Yan, Q., Xin, W., Li, S., and Hua, D.: Detection and analysis of cloud boundary in Xi'an, China, employing 35 GHz cloud radar aided by 1064 nm lidar, Atmospheric Measurement Techniques, 15, 4989–5006, https://doi.org/10.5194/amt-15-4989-2022, 2022.

Zheng, J.-F., Liu, L.-P., Zeng, Z.-M., Xie, X., Wu, J., and Feng, K.: Ka-band millimeter wave cloud radar data quality control, J. Infrared Millim. Waves, 35, 748–757, https://doi.org/10.11972/j.issn.1001-9014.2016.06.018, 2016.